In-situ observations of bubble growth in basaltic, andesitic and rhyodacitic melts

M. Masotta[1,*)], H. Ni[1,2)], H. Keppler[1)]

[1)] *Bayerisches Geoinstitut, Universität Bayreuth, 95440 Bayreuth, Germany*

[2)] *CAS Key Laboratory of Crust-Mantle Materials and Environments, School of Earth and Space Sciences, University of Science and Technology of China, Hefei 230026, China*

***Corresponding author:**

Matteo Masotta

Bayerisches Geoinstitut, Universität Bayreuth, 95440 Bayreuth, Germany

Tel.: +49 (0)921 55 3739

E-mail: matteo.masotta@uni-bayreuth.de

Abstract

Bubble growth strongly affects the physical properties of degassing magmas and their eruption dynamics. Natural samples and products from quench experiments provide only a snapshot of the final state of volatile exsolution, leaving the processes occurring during its early stages unconstrained. In order to fill this gap, we present *in-situ* high-temperature observations of bubble growth in magmas of different compositions (basalt, andesite and rhyodacite) at 1100 to 1240 °C and 0.1 MPa (1 bar), obtained using a moissanite cell apparatus. The data show that nucleation occurs at very small degrees of supersaturaturation (<60 MPa in basalt and andesite, 200 MPa in rhyodacite), probably due to heterogeneous nucleation of bubbles occurring simultaneously with the nucleation of crystals. During the early stages of exsolution, melt degassing is the driving mechanism of bubble growth, with coalescence becoming increasingly important as exsolution progresses. Ostwald ripening occurs only at the end of the process and only in basaltic melt. The average bubble growth rate (G_R) ranges from $3.4*10^{-6}$ to $5.2*10^{-7}$ mm/s, with basalt and andesite showing faster growth rates than rhyodacite. The bubble number density (N_B) at nucleation ranges from $7.9*10^{4}$ mm^{-3} to $1.8*10^{5}$ mm^{-3} and decreases exponentially over time. While the rhyodacite melt maintained a well-sorted bubble-size distribution (BSD) through time, the BSD´s of basalt and andesite are much more inhomogeneous. Our experimental observations demonstrate that bubble growth cannot be ascribed to a single mechanism but is rather a combination of many processes, which depend on the physical properties of the melt. Depending on coalescence rate, annealing of bubbles following a single nucleation event can produce complex bubble size distributions. In natural samples, such BSD´s may be misinterpreted as resulting from several separate nucleation events. Incipient crystallization upon cooling of a magma may allow bubble nucleation already at very small degrees of supersaturation and could therefore be an important trigger for volatile release and explosive eruptions.

Keywords

Bubble growth, bubble coalescence, magma degassing, Ostwald ripening, moissanite cell

1. Introduction

Explosive volcanic eruptions are powered by volatiles exsolving from magmas during their ascent toward Earth's surface. At constant temperature, the solubility of volatile species (mostly H_2O and CO_2) is controlled by pressure and melt composition (Moore et al. 1998; Papale 1999; Liu et al. 2005; Ni and Keppler 2013). The combination of these two parameters determines the depth at which volatiles exsolve from the melt. The expansion of the resulting gaseous phase (i.e., bubbles) controls the effusive or explosive behaviour of magmas during volcanic eruptions. The eruptive style is thus determined by the mechanisms of bubble nucleation and growth (i.e., melt degassing, bubble coalescence, Ostwald ripening), which can be inferred only through bubble size distribution analysis of volcanic rocks or experimental products (e.g., Proussevitch et al. 2007; Shea et al. 2010; Lautze et al. 2011). Unlike crystal phases, the molar volume of the gas phase forming bubbles is much higher than that of the melt, therefore bubbles cannot be treated like crystals in size distribution studies (Proussevitch et al. 2007). Moreover, the higher mobility of the gas phase in the melt as compared to that of crystals implies another limitation for the textural interpretation of volcanic rocks, which only record the last frame of the degassing process. Given these restrictions, experiments with analogue materials have been performed and experimental products have been compared to natural textures (Blower et al. 2002). However, such comparisons rely on scaling assumptions to account for differences in thermal and chemical conditions. These assumptions may not always be valid. For this reason, accurate insights into the exsolution process can be obtained only through direct observations at conditions comparable to those of degassing magmas.

First *in-situ* observations of bubble growth were obtained heating hydrous glassy sample at ambient pressure in heating stages (Bagdassarov et al. 1996; Navon et al. 1998; Liu and Zhang 2000). These studies investigated bubble growth in rhyolitic melts and showed experimental results consistent with the growth laws inferred by theoretical models (Toramaru 1989; Toramaru 1995; Proussevitch et al. 1993; Lyakhovsky et al. 1996). More recently, high-pressure devices were developed and used to investigate *in-situ* bubble growth in silicic melts (Martel and Bureau 2001; Gondé et al. 2006; Gondé et al. 2011). The experimental results were also consistent with observations of natural products, demonstrating the reliability of the experimental approach to the problem of magma vesiculation.

The low experimental temperature (generally well below 1000 °C) and the exclusive use of rhyolitic-type melt compositions are the main limitations of the experiments carried out so far. To overcome these limitations and to advance the investigation of bubble growth to higher temperatures and to basaltic compositions, we present new experimental *in-situ* observations of vesiculation obtained on basalt, andesite and rhyodacite melt compositions at temperature up to 1240 °C, using a recently developed moissanite cell apparatus (Schiavi et al. 2010). This technique was used by Schiavi et al. (2009) to observe the crystallization of a basaltic andesite and it can also be applied to investigate the kinetics of volatile exsolution in magmas. With some improvements of the initial experimental design, we have studied synthetic melts of different composition (basalt, andesite and rhyodacite) to unravel the dynamics of bubble growth in magmas at its early stages.

2. Experimental and analytical methods

2.1 Sample preparation and characterization

We used synthetic glasses as starting material representative for different magma compositions (basalt, andesite and rhyodacite), obtained by melting a mixture of analytical grade oxides, carbonates and nitrates at 1 atm and 1600 °C for two hours in a platinum crucible. After this, basalt and andesite were melted once again under vacuum ($P=10^{-2}$ mbar) at 1500 °C for 4 hours. Resulting glasses were clear and bubble-free, as confirmed with a scanning electron microscope (SEM), see Figure A1 in the electronic appendix. Chemical analyses of these glasses were obtained with a JEOL JXA-8200 electron microprobe, using a 10 μm defocused beam, accelerating voltage of 15 kV and current of 15 nA (Table 1). To improve the optical transparency of the sample, in the basalt and andesite compositions, all FeO was replaced by MnO.

Despite the melting of the starting mixture at atmospheric pressure (rhyodacite) or under vacuum (basalt and andesite), the resulting glasses contained small concentrations of dissolved water (as OH^-) and CO_2 (as carbonate, CO_3^{2-}). Volatile contents in the glasses were measured on 200-1800 μm thick, double polished samples, using a Bruker IFS 120 Fourier transformed infrared (FTIR) spectrometer coupled to an infrared microscope. A narrow-band MCT detector was used together with a tungsten source and a Si-coated CaF_2 beam splitter to measure the 3600 cm^{-1}

band of OH^-, while the same detector was used together with a globar source and a Ge-coated KBr beam splitter to measure the carbonate peak at ca. 1550 cm^{-1}. Water and CO_2 contents were calculated using the molar absorption coefficients reported by Yamashita et al. (1997) and by Ni and Keppler (2013). Results are reported in Table 1, together with the volume that H_2O and CO_2 would occupy if they were entirely exsolved.

2.2 Moissanite cell experiments

The moissanite cell assembly resembles a Bassett-type externally heated diamond anvil cell, with diamond anvils replaced by large moissanite windows (a detailed description is given by Schiavi et al. 2010). A sample (glass disk of ca. 1.8 mm diameter) was sandwiched between two moissanite windows and surrounded by a yttrium-doped ZrO_2 gasket. Two or three concentric coils of Pt_{90}-Rh_{10} wires on pyrophyllite substrates around each window were used for heating (Figure A2). A digital camera placed on a transmission optical microscope (Zeiss Axioscope 40; output to either eyepieces or camera-computer) recorded time-lapse pictures and movies of the sample. Samples from the starting glasses were prepared in 50-100 μm thick, doubly polished disks that were fitted into the gasket and sandwiched between the moissanite windows.

Before heating the sample to *super-liquidus* temperatures (1240 °C basalt, 1200 °C andesite, 1100 °C rhyodacite), the temperature inside the cell was held for a few hours at 650 °C (experiments with rhyodacite) or 800 °C (experiments with basalt and andesite) in order to release strain on the cell and to minimize the deformation of the cell during heating. No pressure was applied to the sample. The temperature was then increased with a rate of 167 °C/min and held constant at 1240 °C for the basalt melt, at 1200 °C for the andesite melt and at 1100 °C for the rhyodacite melt during the entire exsolution process. These temperatures are 10 to 50 °C above the *liquidus* temperature calculated for these melt compositions using MELTS (Ghiorso and Sack 1995). The experiments were terminated after 0.5-7 hours and temperature was rapidly decreased with cooling rates varying from 50 to 100 °C/min. During all the experiment, Ar was flushed through the cell.

Image analysis of bubbles was carried out using the free WEB software package ImageJ (Image Processing and Analysis in Java; http://rsb.info.nih.gov/ij/). Microscope pictures were converted to binary (8 bit) images. To limit the error on

particle counting and measuring, the touching edges of adjacent bubbles were drawn manually. Bubble growth rate (G_R) was calculated in each picture by the average increase of bubble radius over time elapsed since the final run temperature had been reached. The bubble number density (N_B) was calculated in selected pictures from each experiment, using the following equation (Gardner 2007):

$$N_B = \frac{\phi_M}{\sum\left(\left(\frac{n_i}{N_T}\right)V_i\right)} \quad (1)$$

where n_i and V_i are the number and volume of bubbles of diameter i, respectively, N_T is the total number of bubbles and ϕ_M is the porosity, which is calculated as the volume fraction of bubbles in the sample (Gardner et al. 1999):

$$\phi_M = \frac{V_{bubble}}{V_{bubble} + V_{melt}} \quad (2)$$

3. Results

3.1 Bubble nucleation and growth mechanisms

Bubble nucleation occurred in all experiments during heating, beyond the glass transformation temperature, but before reaching the *liquidus* temperature. During melting, all samples became nearly opaque, because of the sudden formation of bubbles and crystal nuclei (Figure 1 a-c). The clarity of images improved significantly a few seconds after the achievement of the set point temperature at t_0, revealing the existence of small bubbles (1-4 μm). During the last stage of the heating process, thermal dilatation of the glassy disks caused a slight deformation of the bubbles at the edge of the sample. This was clearly observed in the experiments performed with the more viscous rhyodacitic melt (Figure 1 d-e; see also video in the electronic appendix). Immediately after relaxation of the melt, bubbles formed in the basalt were slightly larger than those in andesite, and consistently larger than those in rhyodacite (Figure 2).

The opacity of the sample during melting prevented the evaluation of possible effects of the moissanite surface on bubble nucleation. Apparently, bubbles nucleated homogeneously in the sample, since most of the experiments showed small bubbles distributed throughout the thickness of sample and spread all over its area. The

movement of bubbles during the thermal dilatation of the sample also suggests that bubble nucleated in the melt, rather than at the interface with the moissanite. In some experiments with basalt, a decrease of the bubble number density was observed toward the rim of the glassy sample, possibly because some degassing occurred through the outer surface of the sample.

Bubble nucleation occurred exclusively at the beginning of each experiment and was then followed by bubble growth. After relaxation, bubble growth continued without deformation until the bubble achieved a critical diameter, corresponding to the thickness of the glassy disks. At this point, because bubble deformation became significant and menisci formed on the moissanite windows, the experiments were either terminated or the images captured later were not analysed. In terms of bubble growth dynamics, all the experiments showed consistent results independent from the composition of the melt, with melt degassing and coalescence being the prevailing mechanisms of bubble growth. Growth by melt degassing dominated during the very early stages of the experiments whereas bubble coalescence became increasingly important after bubbles had grown enough to interact with each other. The overall increase of porosity over time suggests that exsolution continued throughout the experiments, despite occurring faster at the very beginning of the experiment and eventually decreasing with time. Importantly, none of the experiments considered in this study showed bubbles moving within the melt, which would have favored coalescence. Indeed, thinning and disruption of melt septa between bubbles was the prevailing mechanism of bubble coalescence (Castro et al. 2012). Immediately after the coalescence of two bubbles, the relaxation of the newly formed bubble occurred slightly faster in basalt and andesite than in rhyodacite, but within a few seconds spherical shape was restored (Figure 3; see video in electronic appendix). Coalescence induced an appreciable increase of diameter of the newly formed bubble, with a factor between 1.2 and 1.5, depending on the initial size of the bubbles.

Ostwald ripening occurred towards the end of the experiments (at low values of bubble number density) and only in some experiments performed with basalt. The effect of Ostwald ripening was minor compared to that of coalescence, because it required the presence of bubbles of different size (the distribution in rhyodacite was basically unimodal; Figure 2), with very small bubbles (<10 μm) close to larger ones (>50 μm). These smaller bubbles dissolved in the melt feeding the closest bubbles

without producing an appreciable increase in size, as observed during coalescence (Figure 4).

3.2 Bubble growth rate (G_R) and bubble number density (N_B)

We already pointed out that bubbles that formed in the basaltic melt at the beginning of the experiment were slightly larger than those in andesite, and consistently larger than those in rhyodacite. This reflects the difference of growth rates in melts of different composition. According to our experiments, bubble growth follows a linear law ($r = G_R*t + c$), with a slope that progressively decreases from basalt to rhyodacite (Figure 5 a). Bubble growth rates (G_R), which are given by the slope of the linear fit, are therefore $3.4*10^{-6}$ mm/s, $1.8*10^{-6}$ mm/s and $5.2*10^{-7}$, for basalt, andesite and rhyodacite, respectively (Table 2). The linear law closely describes bubble growth for t>20 s, but cannot be used to predict bubble size at the very beginning of the exsolution (when the opacity of the sample prevented the clear observation of the process). It is clear, however, that bubble growth at this stage was extremely fast (bubbles of several microns had already formed a few seconds after the achievement of the experimental temperature). Hence, the classical formulation of bubble growth with the bubble radius proportional to the square root of time (Sparks 1978; Toramaru 1989; Bottinga and Javoy 1990; Proussevich and Sahagian 1998), or the logarithmic law proposed by Martel and Bureau (2001), may be more adequate in describing bubble growth at the very beginning of exsolution. The contrast between bubble growth at the beginning of the exsolution process and at a later stage implies a significant decrease of G_R shortly after the beginning of exsolution. At t>20 s, G_R remains constant through time (Figure 5 b).

The bubble number density (N_B) decreases with time following an exponential function (Table 2; Figure 6 a). The value of N_B at nucleation can be obtained by the intercept of the curves with the zero-time of the experiments, yielding values of $1.8*10^5$ mm^{-3} for rhyodacite, to $9.5*10^4$ mm^{-3} for basalt and $7.9*10^4$ mm^{-3} for andesite. The shifting of the N_B curves can be related to the different rate of bubble coalescence observed in the three melt compositions, with the rhyodacite showing the slowest rate and the highest density of bubbles. By close approximation (assuming a negligible effect of Ostwald ripening), the bubble coalescence rate (C_R) can be expressed as the negative derivative of N_B with respect to time (Figure 6 b):

$$C_R = -\frac{dN_B}{dt} \quad (3)$$

Unlike for N_B, the C_R cannot be extrapolated for t<20 s, because at this stage melt degassing is the prevailing mechanism and coalescence is not likely to start before bubbles grew enough to interact with each other.

3.3 Bubble size distribution

Bubble size distribution curves are reported in Figure 7 where they are represented by the frequency of bubbles within a specific size class (based on the area of the bubble) and in Figure 8 where they are reported as cumulative distributions of volumetric classes (following the representation of Bai et al. 2008).

The faster bubble growth and coalescence rates in basalt and andesite produced less homogeneous bubble size distributions than in rhyodacite. In basalt, bubbles rapidly evolve from a polymodal distribution to a poorly sorted distribution with a positive skew and a mode between 64 and 128 μm^2 (Figure 7 a). In andesite, bubble growth proceeds with a rate similar to that of basalt, but bubbles achieve a bimodal distribution (Figure 7 b). The slowest growth rate produced in rhyodacite the most sorted distribution with a mode shifting through time toward larger bubble sizes and a tail developing toward left (Figure 7 c).

Cumulative bubble size distributions show trends comparable with those obtained by X-ray micro-tomography of high-pressure experiments (Bai et al. 2008) and display exponential law relations, independent of melt composition and vesicularity (Figure 8). The exponential law relation closely matches the bubble size distribution of rhyodacite; however, in both basalt and andesite the central segment of the curve rather seems to follow a power law relation, which rotates counterclockwise with time around the volume of 1000 μm^3. This trend is remarkably similar to that observed in crystal size distributions studies and actually reveals a difference in growth rate between the smaller bubbles and the larger ones.

4. Discussion

4.1 Effect of volatile saturation on bubble nucleation

According to the data in Table 1, the amount of H_2O in our samples (10-20 ppm in basalt and andesite and ca. 400 ppm in rhyodacite) is small compared to the amount of dissolved CO_2 in the melt. The complete exsolution of the H_2O dissolved in each sample alone would be sufficient at 0.1 MPa to produce a gas phase with a volume comparable or greater than the measured volume of bubbles. Most likely, however, CO_2, which is relatively abundant in the melt compared to water, is the main component of the gas phase exsolved during our experiments.

The supersaturation pressure (ΔP) is defined as the difference between the saturation pressure of the volatile species dissolved in the melt and the pressure at which bubble nucleation occurs. In our experiments bubbles nucleate at 0.1 MPa and the supersaturation pressure corresponds approximately to the saturation pressure of the CO_2 present in our samples, ignoring the much smaller contribution of water. Based on the interpolation of several CO_2 solubility studies, Ni and Keppler (2013; and references therein) found that CO_2 solubility increases with pressure linearly following a slope 5.67 ppm CO_2/MPa (almost independent of melt composition). Using this relation, we can roughly calculate ΔP values of 18, 51 and 200 MPa for basalt, andesite and rhyodacite, respectively. The values obtained for basalt and andesite are smaller than those reported in previous studies for homogeneous nucleation (e.g., Gondé et al. 2011). Mourtada-Bennefoi and Laporte (2002) found that the degree of supersaturation in rhyolitic magmas increases for decreasing concentration of H_2O and increasing concentration of CO_2. According to these authors, minimum ΔP values (27-94 MPa) are obtained with 630 ppm of CO_2 and 7 wt.% H_2O, whereas at reduced water content (4.6 wt.%) and higher CO_2 (800 ppm) ΔP increases over 160 MPa. Therefore, we should expect to observe bubble nucleation in the basalt at ΔP higher than 18 MPa. For rhyodacite, ΔP is about one order of magnitude higher than for basalt, but this value may still be too low to produce homogeneous nucleation in nearly dry melts (ΔP is roughly 150 MPa in water-rich melts; Mourtada-Bennefoi and Laporte 1999; Mangan and Sisson 2000; Mourtada-Bennefoi and Laporte 2004). Indeed, the fact that the rhyodacitic melt (as also the basalt and the andesite) did not degas to equilibrium during melting at 1600 °C, suggests that the ΔP was not sufficient for bubble nucleation.

The effect of CO_2 concentration on ΔP has never been investigated in detail in water-poor systems and, in most of CO_2-bearing experiments, this effect was probably hidden by the dominant presence of water. Bai et al. (2008) found that no significant

effect is observed in basalt at CO_2 concentrations within few hundreds ppm, whereas the effect becomes noticeable at concentration higher than 800 ppm.

In the classic theory of bubble nucleation, the ΔP is given by (Hirth et al. 1970; Hurwitz and Navon 1994):

$$\Delta P = \sqrt{\frac{16\pi\sigma^3}{3kT\ln\left(\frac{J_0}{J}\right)}} \quad (4)$$

where σ is the surface tension, k is the Boltzman constant, T is the temperature, J is the nucleation rate and J_0 is a parameter depending on a number of other parameters characteristic for the volatile species dissolved. According to this equation, the elevated temperatures in our experiments, as compared to many other experiments, could have somehow reduced supersaturation pressure. This effect, however, is expected to be rather small. A more likely explanation for the rapid bubble nucleation and the small supersaturation pressures we observe is that the nucleation occurred during heating shortly before reaching the *liquidus* temperature and may have coincided with the nucleation of crystals, which dissolved again upon further heating (Figure 1). Crystal nuclei may have different atomic arrangements and different surface properties than macroscopic crystals, which could explain why the supersaturation pressures we observe are very small. Our observations are, however, completely consistent with the study of Hurwitz and Navon (1994), who showed that the presence of microlites can reduce supersaturation pressures in hydrous rhyolite melts to values as low as 1 MPa. To demonstrate that bubble nucleation in our experiments was likely related to incipient crystallization, we heated some glass chips of our starting materials in a furnace with the same heating rate as in the moissanite cell experiments, but quenched the sample after the glass transformation temperature had been exceeded. Investigation of these samples showed the nucleation of bubbles on the surface of newly formed crystals (Figure A3 in the electronic appendix).

The effect of heterogeneous nucleation may also explain, why bubble nucleation still occurred in experiments with basalt and andesite despite the fact that these samples had been held for 1600 °C in air and in vacuum for several hours. At these *super-liquidus* temperatures, crystal nuclei were not present and heterogeneous nucleation was impossible. Therefore, bubbles could only form by homogeneous nucleation, which requires much higher supersaturation pressures, so that part of the volatiles remained dissolved in the melt. The higher volatile content of the rhyodacite

is related to the fact that it was only molten in air, not in vacuum; this imposes higher supersaturation pressures in the subsequent moissanite cell experiments.

4.2 Bubble growth and evolution of bubble size distribution

Evaluating the contribution of each bubble growth mechanism from the texture of volcanic rocks is challenging, since the traces of these mechanisms are commonly obliterated during the emplacement of the magma (e.g., deformation and channeling of vesicles during the ascent of the magma in the conduit; Bouvet de Maisonneuve et al. 2009). However, in some cases, bubble size distribution studies can be used to assess the occurrence of certain mechanisms of bubble growth (Shea et al. 2010). *In-situ* observations provide valuable insights into the effect of growth mechanisms on bubble size distributions. To overcome the analytical problem of tracking each single growth mechanism (melt degassing, bubble coalescence and Ostwald ripening) and thus, to provide a more direct comparison to natural textures, we have measured the growth of bubbles based on their average size at different times during the experiment.

All experiments show a fast bubble growth, prompted by melt degassing shortly after nucleation (<20 s), and a nearly linear growth for the rest of the experiment, dominated by bubble coalescence (Figure 5 a). As result, bubble growth rates decrease rapidly in the first 20 s (by roughly two orders of magnitude), and then they remain nearly constant for the rest of the experiment (Figure 5 b). The fast initial growth is consistent with experimental data by Gondé et al. (2011), who reported a logarithmic growth law in the first 10 s of the experiment, with an average growth rate of $4.5*10^{-4}$ mm/s (i.e., same order of magnitude as we observe for basalt and andesite after 30 and 45 s, respectively; Table 2). Probably due to limitations of the experimental setup, the authors did not report data for time >10 s. However, a prolonged *in-situ* observation is reported in Bagdassarov et al. (1996) who, consistent with our results, found a decrease of bubble growth rates with time. Similarly, Bai et al. (2008), using microtomographic *in-situ* measurements, observed that bubble growth was faster in the first 10-20 s and then progressively decreased with time. In general, the classic theory of bubble growth (where $R \sim t^{1/2}$; Proussevich and Sahagian 1998) offers a good approximation to these experimental observations, despite the magnitude of the process may be dependent on factors like the amount of volatiles dissolved and the composition of the melt. On the other hand, theoretical model

cannot be used to predict the bubble size distribution (BSD) and its evolution with time, but rather, *in-situ* experiments provide the more reliable evidence on how bubble growth mechanisms affect the evolution of BSD.

The three melt compositions showed a different evolution of the BSD, with basalt and rhyodacite showing the least and most sorted distribution, respectively (Figure 7). During all the experiments, the distribution of bubbles in the rhyodacitic melt remained more homogeneous than in basalt and andesite, which, on the contrary, evolved into poorly sorted distributions (Figure 2, Figure 7). The close fit of the exponential law to the cumulative distribution of rhyodacite evidences the higher homogeneity of the BSD, compared to basalt and andesite, whose cumulative distributions can be fitted by a power law in the intermediate region (Figure 8). Such variability of BSD can be related to the variable rate of coalescence in the three melt compositions. Specifically, faster rates of bubble coalescence (i.e., experiments with basalt and andesite) are likely to produce much more heterogeneous distributions than for slow rates (i.e., experiment with rhyodacite).

The striking effect of the coalescence rate C_R in modifying the BSD curves may easily lead to a misinterpretation of the texture of volcanic rocks. For example, the occurrence of multiple modes in the BSD of basalt and andesite (Figure 7) could be interpreted by means of secondary nucleation events (Klug et al. 2002; Polacci et al. 2003; Lautze and Houghton 2007) that actually did not occur during the experiments. Rather, our observations suggest that the faster C_R in these two melts amplified the effect of proportionate growth (i.e., growth rate proportionate to the size of the bubble) that, shortly after the beginning of vesiculation, produced right skews and multiple modes in the BSD. Proportionate growth is also visible in the BSD of rhyodacite, the left tail of which indicates the persistence of small bubbles that grew much less than larger ones, as a result of the much slower C_R of this melt, as compared to basalt and andesite.

4.3 Evolution of bubble number density (N_B)

The initial bubble number density at nucleation can be estimated by extrapolating the curves for N_B to the time zero of the experiment (Figure 6 a). These values range from $7.9*10^4$ to $1.8*10^5$ mm^{-3} and match previous determinations of N_B obtained by *in-situ* experiments on H_2O-saturated haplogranitic composition (Gondé et al. 2011). However, considering the differences in volatile content, temperature,

pressure and nucleation mechanism, this agreement may be fortuitous. Bulk volatile concentration will influence the evolution of N_B over time, with high volatile contents causing a faster decrease of N_B (Gardner et al. 1999). Accordingly, N_Bs calculated in our experiments are up to two orders of magnitude higher than N_Bs reported in literature for experimentally decompressed H_2O-saturated dacitic and rhyolitic melts (Gardner and Ketcham 2011), as expected from the low volatile content of the melt.

Our experimental determinations of N_B overlap the values typical of natural pumices, ranging between 10^4 and 10^7 mm^{-3} (Polacci et al. 2001; Klug et al. 2002; Colucci et al. 2013), whereas they are higher than N_B of less explosive products, which typically range between 10^1 and 10^3 mm^{-3} (Parcheta et al. 2013).

4.4 Effect of temperature and melt composition on volatile exsolution

Bubble nucleation density and growth rates are controlled by the volatile diffusivity of the melt that, in turn, depends on the polymerization of the melt (NBO/T). This is because nuclei of bubbles need to exceed critical size to continue to grow spontaneously and even a bubble of 0.1 μm size contains in the order of 10^6 molecules of CO_2 or H_2O, which have to be transported to the bubble by diffusion. Melt characterized by lower diffusivity are likely to be characterised by higher N_B at nucleation, because of the smaller volume of melt feeding each bubble. Consistently, the experiment performed with rhyodacite at 1100 °C showed higher N_B than the experiments with andesite and basalt performed at 1200 and 1240 °C, respectively, and another experiment performed with rhyodacite at 1200 °C. For CO_2, however, bulk composition and NBO/T may have only a minor effect on diffusivity (Zhang and Ni 2010). In this regard, it should be noted that the variation of N_B at nucleation in the three compositions is within one order of magnitude, which is much less than the overall variability observed in natural products. Rather, the difference of N_B among the melt compositions investigated, in particular between basalt and rhyodacite, increases with time. Therefore, with the increasing bubble size and interaction between bubbles, melt viscosity probably controls the rates of bubble growth and coalescence. In fact, despite the considerably higher degree of supersaturation, rhyodacite shows remarkably slower growth and coalescence rates as compared to the less viscous basaltic and andesitic melt.

4.5 Implications for volcanic systems

Degassing-induced crystallization is common in magmas experiencing syn-eruptive decompression (Mastrolorenzo and Pappalardo 2006; Humpreys et al. 2008; Brophy 2009; Martel 2012; Mollard et al. 2012). Our experiments suggest that there may also be a reverse relationship, with crystal nucleation being a possible cause of bubble nucleation. Indeed, bubble nucleation in basalt and andesite occurs despite the relatively small degree of volatile supersaturation of the melt, because of the presence of crystal nuclei that act as nucleation sites for bubble (Hurwitz and Navon 1994). By analogy to our experimental observations, the incipient crystallization of a magma upon cooling may trigger volatile release and possibly, explosive volcanic eruptions. This situation is likely to occur in differentiating magmas that achieve a pseudo-invariant temperature that, once crossed, undergo to significant increase of crystallization (Fowler et al. 2007). An alternative scenario could be the emplacement and cooling of a crystal-poor magma at shallow depths. Here, the very onset of crystallization could trigger an eruption. The very high bubble number densities at relatively small supersaturation that we observe in our experiments, suggest that this mechanism could be quite important in nature. We also observe how melts of lower viscosity (basalt and andesite) rapidly achieve heterogeneous bubble distributions and a less dense bubble packing than high viscous ones. Indeed, melts of higher viscosity (rhyodacite) are likely to maintain a denser bubble packing for longer time, being thus more susceptible to brittle failure and fragmentation, when the tensile stress at the inner walls of bubbles exceeds the tensile strength of the magma (Zhang 1999).

5. Conclusions

Moissanite cell experiments allowed the direct observation of bubble nucleation and growth at magmatic conditions that are otherwise not directly accessible. The data presented in this study are therefore complementary to studies of bubble growth performed at high-pressure and/or using controlled decompression rates. Our experiments suggest that bubbles can nucleate at very small degrees of supersaturation simultaneously with the nucleation of crystals. This implies that incipient crystallization upon magma cooling could be an important mechanism for triggering volatile release and explosive eruptions already at small degrees of volatile supersaturation.

Melt polymerization plays role in determining the bubble number density at nucleation, whereas, the viscosity of the melt controls the rates of bubble growth and coalescence. Magmas characterized by higher NBO/T and lower viscosity are likely to exhibit lower bubble number density at nucleation and faster growth and coalescence rates, compared to magmas characterized by lower NBO/T and higher viscosity. As result, bubble size distribution curves may evolve to very different shapes, from multi-modal, in the case of less viscous magmas, to well sorted, in the case of the more viscous ones. Such variability remarks the striking effect of coalescence in changing the bubble size distributions, which may easily yield to misinterpreting the texture of natural rocks.

Aknowledgments

We are grateful to Hubert Schulze and Raphael Njul for sample preparation, Sven Linhardt for technical assistance, Detlef Krauße, Ulrike Trenz and Florian Heidelbach for assistance during EMPA and SEM analyses. Insightful comments from the Editor and two anonymous reviewers greatly improved the manuscript. This work was supported by Humboldt fellowship to MM.

References

Bagdassarov NS, Dingwell DB, Wilding MC (1996) Rhyolite magma degassing: an experimental study of melt vesiculation. Bull Volcanol 57:587-601

Bai L, Baker DR, Rivers M (2008) Experimental study of bubble growth in Stromboli basalt melts at 1 atm. Earth Planet Sci Lett 267:533-547

Blower JD, Keating JP, Mader HM, Phillips JC (2002). The evolution of bubble size distributions in volcanic eruptions. J Volcanol Geotherm Res 120:1-23

Bottinga Y, Javoy M (1990) MORB degassing: Bubble growth and ascent. Chem Geol, 81:225-270

Bouvet de Maisonneuve C, Bachmann O, Burgisser A (2009) Characterization of juvenile pyroclasts from the Kos Plateau Tuff (Aegean Arc): insights into the eruptive dynamics of a large rhyolitic eruption. Bull Volcanol 71:643-658

Brophy JG (2009) Decompression and H_2O exsolution driven crystallization and fractionation: development of a new model for low pressure fractional

crystallization in calc-alkaline magmatic systems. Contrib Mineral Petrol 157:797-811

Castro JM, Burgisser A, Schipper CI, Mancini S (2012) Mechanisms of bubble coalescence in silicic magmas. Bull Volcanol 74:2339-2352

Colucci S, Palladino DM, Mulukutla GK, Proussevitch AA (2013) 3-D reconstruction of ash vesicularity: Insights into the origin of ash-rich explosive eruptions. J Volcanol Geotherm Res 255:98-107

Fowler SJ, Spera F, Bohrson W, Belkin HE, De Vivo B (2007) Phase equilibria constraints on the chemical and physical evolution of the Campanian Ignimbrite. J Petrol 48:459-493

Gardner JE, Hilton M, Carroll MR (1999) Experimental constraints on degassing of magma: isothermal bubble growth during continuous decompression from high pressure. Earth Planet Sci Lett 168:201-218

Gardner JE (2007) Bubble coalescence in rhyolitic melts during decompression from high pressure. J Volcanol Geotherm Res 166:161-176

Gardner JE, Ketcham RA (2011) Bubble nucleation in rhyolite and dacite melts: temperature dependence of surface tension. Contrib Mineral Petrol 162:929-943

Ghiorso MS, Sack RO (1995) Chemical mass transfer in magmatic processes. IV. A revised and internally consistent thermodynamic model for the interpolation and extrapolation of liquid-solid equilibria in magmatic systems at elevated temperatures and pressures. Contrib Mineral Petrol 119:197-212

Gondé C, Massare D, Bureau H, Martel C, Pichavant M, Clocchiatti R (2006) In situ study of magmatic processes: a new experimental approach. High Press Res 26:243-250

Gondé C, Martel C, Pichavant M, Bureau H (2011) In situ bubble vesiculation in silicic magmas. Am Mineral 96:111-124

Hirth JP, Pound GM, StPierre GR (1970) Bubble nucleation. Met Trans 1:939-945

Humphreys MCS, Blundy JD, Sparks RSJ (2008) Shallow-level decompression crystallization and deep magma supply at Shiveluch Volcano. Contrib Mineral Petrol 155:45-61

Hurwitz S, Navon O (1994) Bubble nucleation in rhyolitic melts: experiments at high pressure, temperature, and water content. Earth Planet Sci Lett 122:267-280

Klug C, Cashman KV, Bacon CR (2002) Structure and physical characteristics of pumice from the climatic eruption of Mount Mazama (Crater Lake), Oregon. Bull Volcanol 64:486-501

Lautze NC, Houghton BF (2007) Linking variable explosion style and magma textures during 2002 at Stromboli volcano, Italy. Bull Volcanol 69:445-460

Lautze NC, Sisson TW, Mangan MT, Grove TL (2011) Segregating gas from melt: an experimental study of the Ostwald ripening of vapor bubbles in magmas. Contrib Mineral Petrol 161:331-347

Liu Y, Zhang Y (2000) Bubble growth in rhyolitic melt. Earth Planet Sci Lett 181:251-264

Liu Y, Zhang Y, Behrens H (2005) Solubility of H_2O in rhyolitic melts at low pressures and a new empirical model for mixed H_2O–CO_2 solubility in rhyolitic melts. J Volcanol Geotherm Res 143:219-235

Lyakhovsky V, Hurwitz S, Navon O (1996) Bubble growth in rhyolitic melts: experimental and numerical investigation. Bull Volcanol 58:19-32

Mangan MT, Sisson TW (2000) Delayed, disequilibrium degassing in rhyolite magma: decompression experiments and implications for explosive volcanism, Earth Planet Sci Lett 183:441-455

Martel C, Bureau H (2001) In situ high-pressure and high-temperature bubble growth in silicic melts. Earth Planet Sci Lett 191:115-127

Martel C (2012) Eruption dynamics inferred from microlite crystallization experiments: application to plinian and dome-forming eruptions of Mt. Pelée (Martinique, Lesser Antilles). J Petrol 53:699-725

Mastrolorenzo G, Pappalardo L (2006) Magma degassing and crystallization processes during eruptions of high-risk Neapolitan-volcanoes: evidence of common equilibrium rising processes in alkaline magmas. J Volcanol Geotherm Res 83:219-239

Moore G, Vennemann T, Carmichael ISE (1998) An empirical model for the solubility of H_2O in magmas to 3 kilobars. Am Mineral 83:36-42

Mollard E, Martel C, Bourdier J (2012) Decompression-induced crystallization in hydrated silica-rich melts: empirical models of experimental plagioclase nucleation and growth kinetics. J Petrol 53:1743-1766

Mourtada-Bonnefoi, CC, Laporte D (1999) Experimental study of homogeneous bubble nucleation in rhyolitic magmas. Geophys Res Lett 26:3505-3508

Mourtada-Bonnefoi CC, Laporte D (2002) Homogeneous bubble nucleation in rhyoliticmagmas: an experimental study of the effect of H_2O and CO_2. J Geophys Res 107:B4

Mourtada-Bonnefoi CC, Laporte D (2004) Kinetics of bubble nucleation in a rhyolitic melt: an experimental study of the effect of ascent rate. Earth Planet Sci Lett 218:521537

Navon O, Chekhmir A, Lyakhovsky V (1998) Bubble growth in highly viscous melts: theory, experiments, and autoexplosivity of dome lavas Earth Planet Sci Lett 160:763-776

Ni HW, Keppler H (2013) Carbon in Silicate Melts. In: Hazen RM, Jones AP, Baross JA (Eds.), Carbon in Earth Rev Mineral Geochem 75:251-287

Ni HW, Keppler H, Walte N, Schiavi F, Masotta M, Chen Y, Cheng ZJ (2013) Crystallization of a High-K Basaltic Melt Observed with the Moissanite Cell. Geology, submitted.

Papale P (1999) Modeling of the solubility of a two-component H_2O+CO_2 fluid in silicate liquids. Am Mineral 84:477-492

Parcheta CE, Houghton BF, Swanson DA (2013) Contrasting patterns of vesiculation in low, intermediate, and high Hawaiian fountains: A case study of the 1969 Mauna Ulu eruption. J Volcanol Geotherm Res 255:79-89

Polacci M, Papale P, Rosi M (2001) Textural heterogeneities in pumices from the climactic eruption of Mount Pinatubo, 15 June 1991, and implication for magma ascent dynamics. Bull Volcanol 63:83-97

Polacci M, Pioli L, Rosi M (2003) The Plinian phase of the Campanian Ignimbrite eruption (Phlegrean Fields, Italy): evidence from density measurements and textural characterization of pumice. Bull Volcanol 65:418-432

Proussevitch AA, Sahagian DL, Anderson AT (1993) Dynamics of diffusive bubble growth in magmas: Isothermal case. J Geophys Res 98:22283-22307

Proussevitch AA, Sahagian DL (1998) Dynamics and energetics of bubble growth in magmas: Analytical formulation and numerical modeling. J Geophys Res 103:18223-18251

Proussevitch AA, Sahagian DL, Carlson WD (2007) Statistical analysis of bubble and crystal size distributions: Application to Colorado Plateau basalts. J Volcanol Geotherm Res 164:112-126

Schiavi F, Walte N, Keppler H (2009) First in situ observation of crystallization processes in a basaltic-andesitic melt with the moissanite cell. Geology 37:963-966

Schiavi F, Walte N, Konschak A, Keppler H (2010) A moissanite cell apparatus for optical in situ observation of crystallizing melts at high temperature. Am Mineral 95:1069-1079

Shea T, Houghton BF, Gurioli L, Cashman KV, Hammer JE, Hobden BJ (2010) Textural studies of vesicles in volcanic rocks: An integrate methodology. J Volcanol Geotherm Res, 190:271-289

Sparks RSJ (1978) The dynamics of bubble formation and growth in magmas: a reiew and analysis. J Volcanol Geotherm Res 3:1-37

Toramaru A (1989) Vesiculation process and bubble size distributions in ascending magmas with constant velocities. J Geophys Res 94:17523-17542

Toramaru A (1995) Numerical study of nucleation and growth of bubbles in viscous magmas. J Geophys Res 100:1913-1931

Yamashita S, Kitamura T, Kusakabe M (1997) Infrared spectroscopy of hydrous glasses of arc magma compositions. Geochem J 31:169-174

Zhang Y (1999) A criterion for the fragmentation of bubblymagma based on brittle failure theory. Nature 402:648-650

Zhang Y, Ni H (2010) Diffusion of H, C, and O components in silicate melts. In: Zhang Y, Cherniak D, (Eds.), Diffusion in minerals and melts. Rev Mineral Geochem 72:171-225

Figure captions

Figure 1 – Sequence of pictures of a moissanite cell experiment with rhyodacite showing the moment of bubble nucleation close to the final experimental temperature of 1100 °C (a-c), bubble expansion following the dilatation of the sample (d-e) and contraction immediately afterwards (f-h). The time is given relative to the time t_0, at which the temperature of the set point was reached.

Figure 2 – Snapshots of the experiments performed in moissanite cells using 50 μm thick glassy disks of synthetic basalt (top), andesite (middle) and rhyodacite (bottom). Bubbles in basalt and andesite show less homogeneous distributions than in

rhyodacite and less spherical shape, as results of the faster growth and the higher rate of coalescence. Note the different time necessary to achieve comparable bubble size and the different distribution of bubbles. Arrows indicate bubbles in the process of coalescence.

Figure 3 – Sequence of pictures showing the coalescence of bubbles in rhyodacitic melt at 1200 °C, as indicated by the arrows. Frames are taken in 1 s intervals. The shapes of coalesced bubbles change from elliptical to spherical within few seconds.

Figure 4 - Sequence of pictures of an experiment performed with basalt, showing the occurrence of Ostwald ripening. Compared to coalescence, Ostwald ripening is much slower and involves bubbles of different size. The small bubbles near the larger one in the top right corner (red arrows) are redissolved in the melt causing a slightly perceptible increase of the volume of the large bubble.

Figure 5 – (a) Linear fitting of bubble size through time ($t>20$ s). Bubble growth at $t<20$ s occurs much faster than after 20 s and can be approximated by a logarithmic law. (b) Bubble growth rates (G_R) calculated by the derivative with respect to time of the growth laws.

Figure 6 – (a) Variation of bubble number density (N_B) and (b) coalescence rate (C_R) with time. The coalescence rate expresses the number of coalescence events ($mm^{-3}*s^{-1}$) and is calculated from the derivative of the N_B curves with respect to time.

Figure 7 – Evolution of bubble size distribution (BSD) through time for the three different melt compositions. The area of the bubble is plotted instead of the radius, in order to increase the number of bins that can be plotted and to reduce the error of the determination of the radius from the area obtained from image analyses. Each bin corresponds to a class of bubble area calculated on basis 2 (e.g., 0-2 μm^2, 2-4 μm^2, 4-8 μm^2, etc.). Note how distributions in basalt and andesite achieve in a relatively short time poorly sorted distributions, whereas rhyodacite maintains through time a well-sorted distribution.

Figure 8 – Log-Log plot of cumulative bubble size distribution. The number of bubbles is normalized to the volume of the sample. The overall distribution follows an exponential law for all the three compositions, with the rhyodacitic melt showing the best fitting (panels on the left). In the central segment, the distribution of basalt and andesite show the best fitting with a power law, which exponential term increases with time producing a counterclockwise rotation of the fitting line (panels on the right).

Figure 1
Click here to download high resolution image

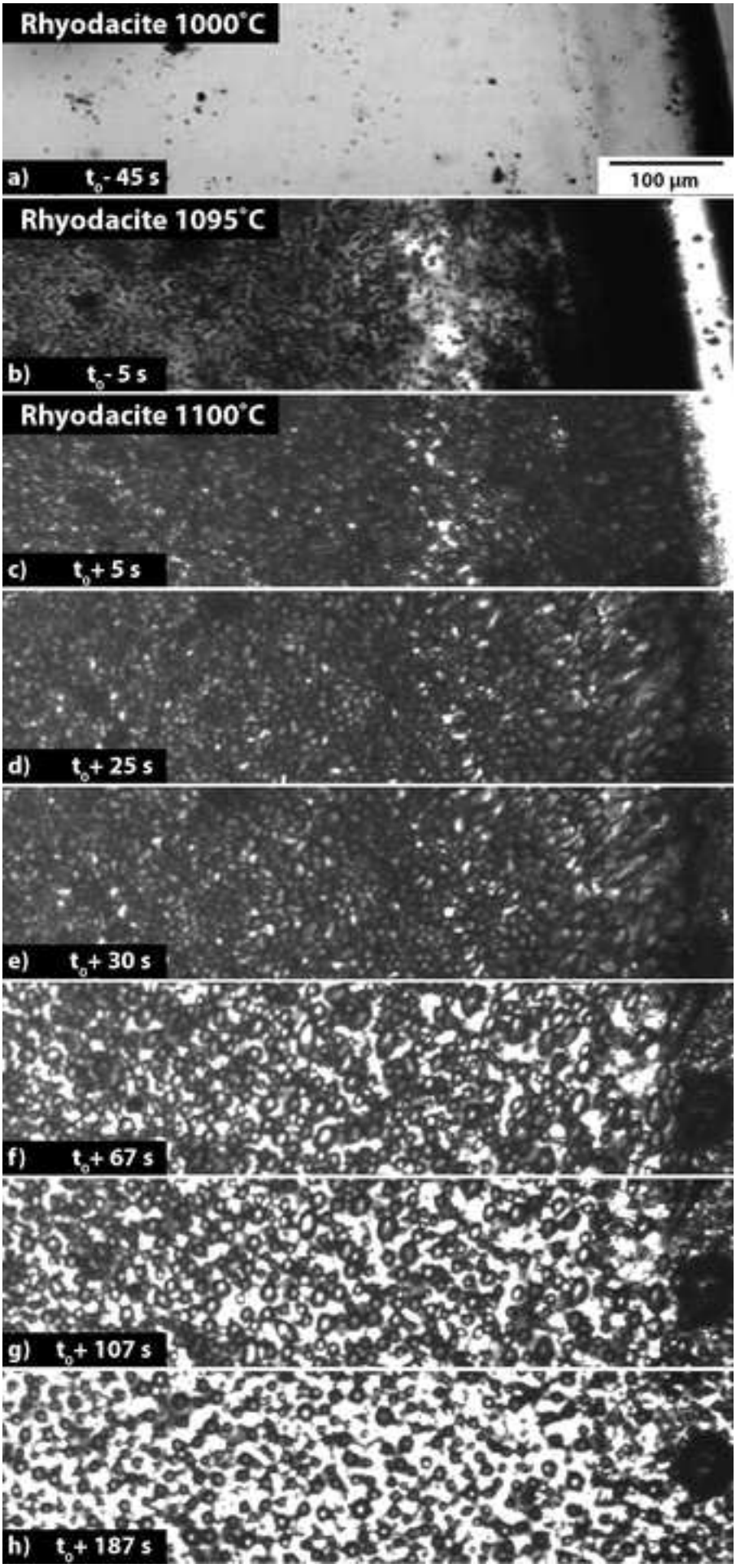

Figure 2
Click here to download high resolution image

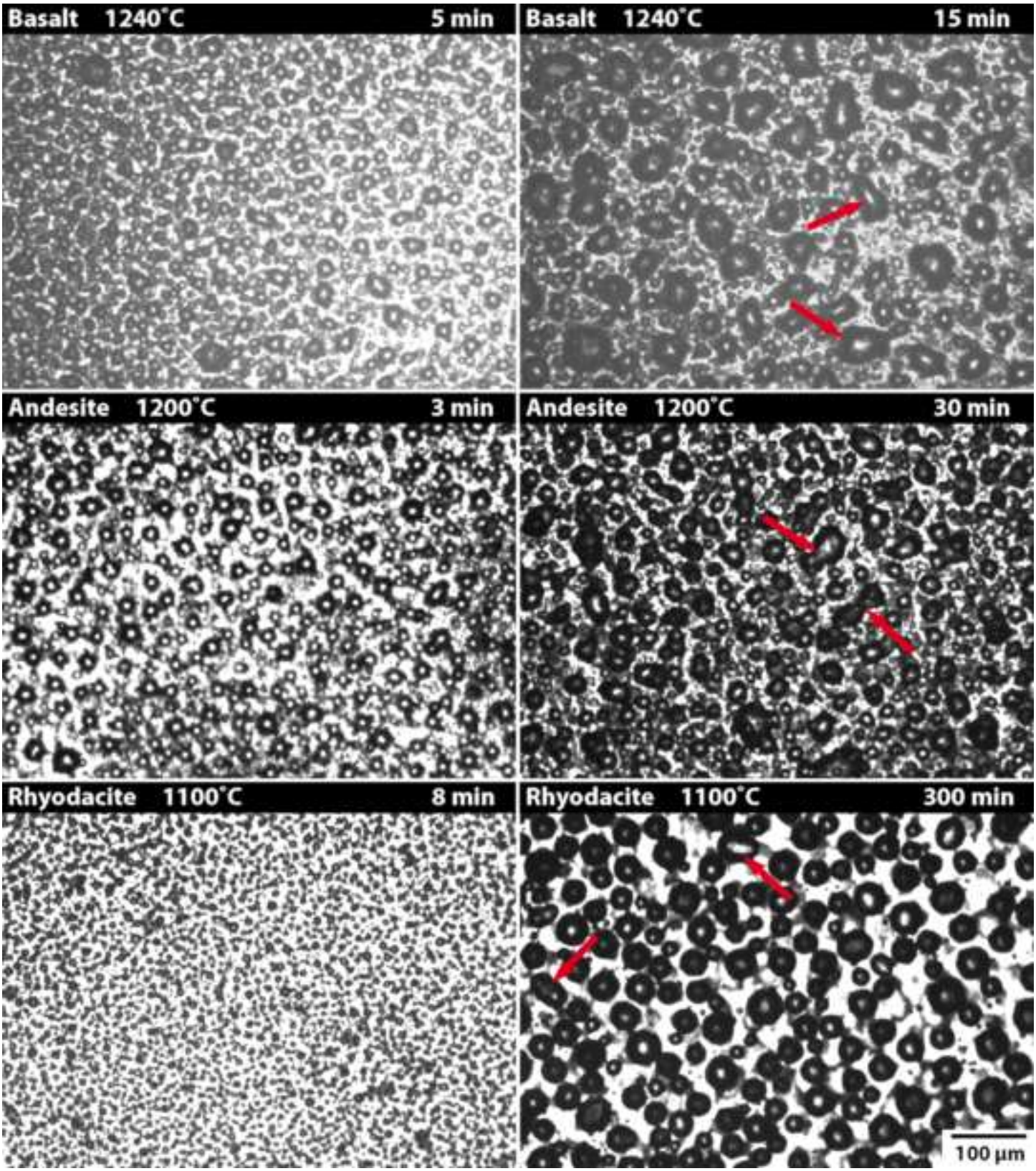

Figure 3
Click here to download high resolution image

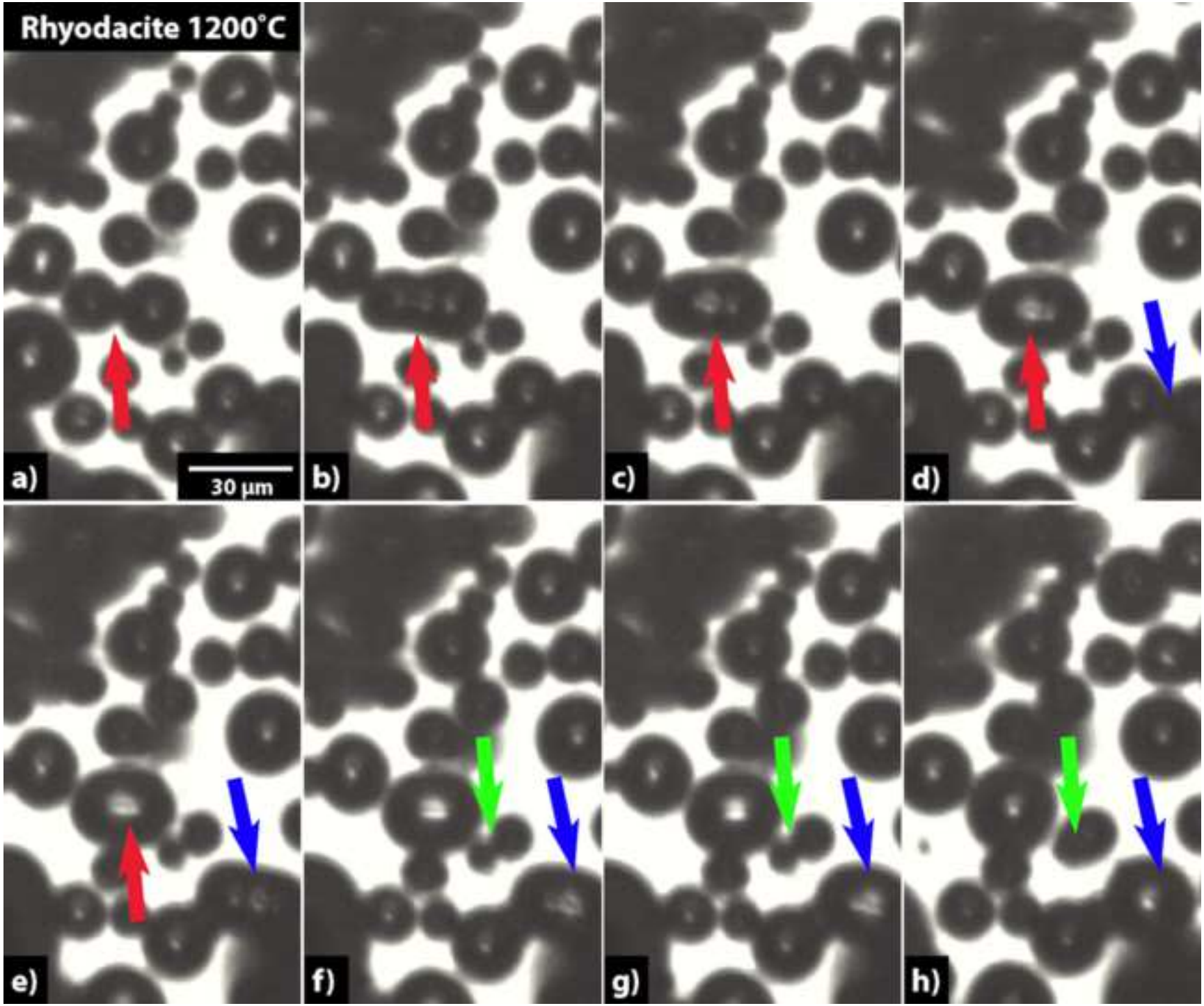

Figure 4
Click here to download high resolution image

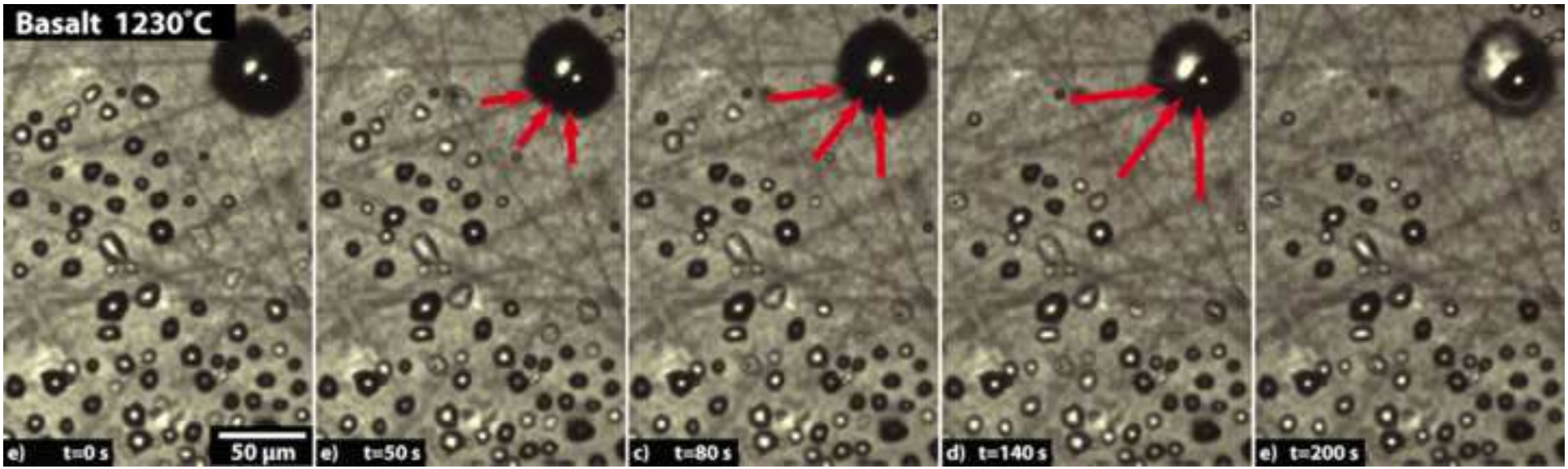

Figure 5
Click here to download high resolution image

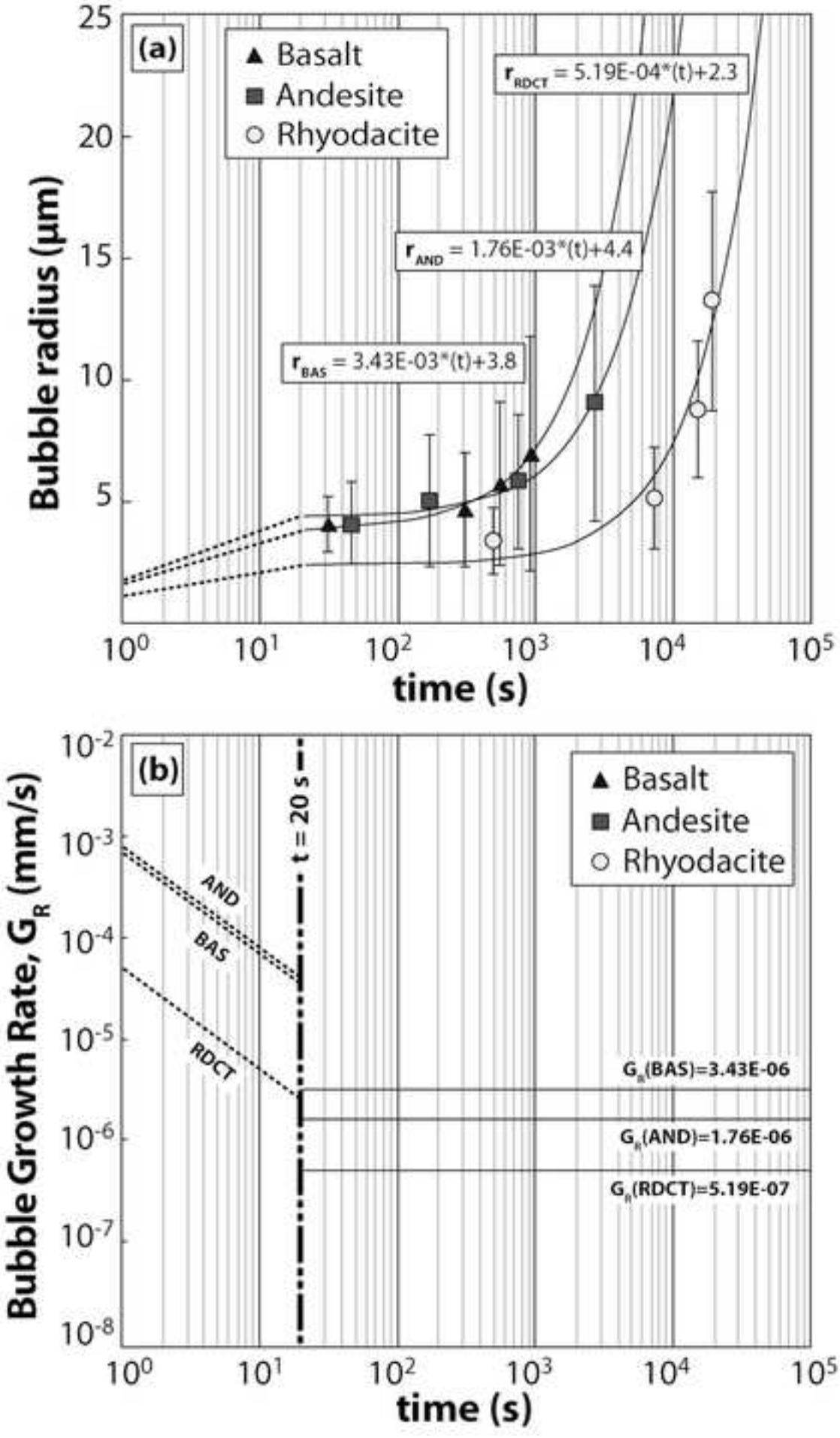

Figure 6
Click here to download high resolution image

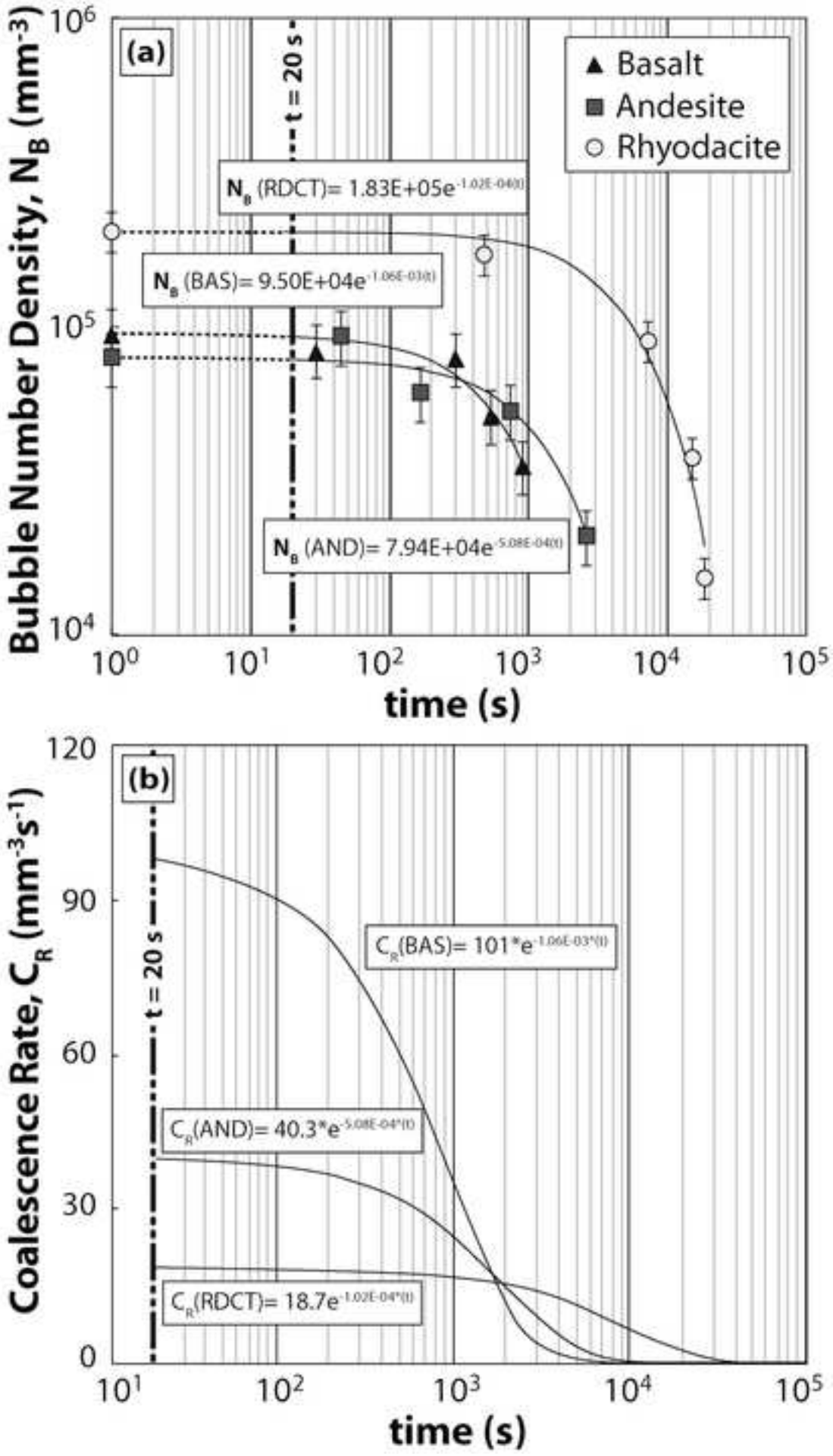

Figure 7
Click here to download high resolution image

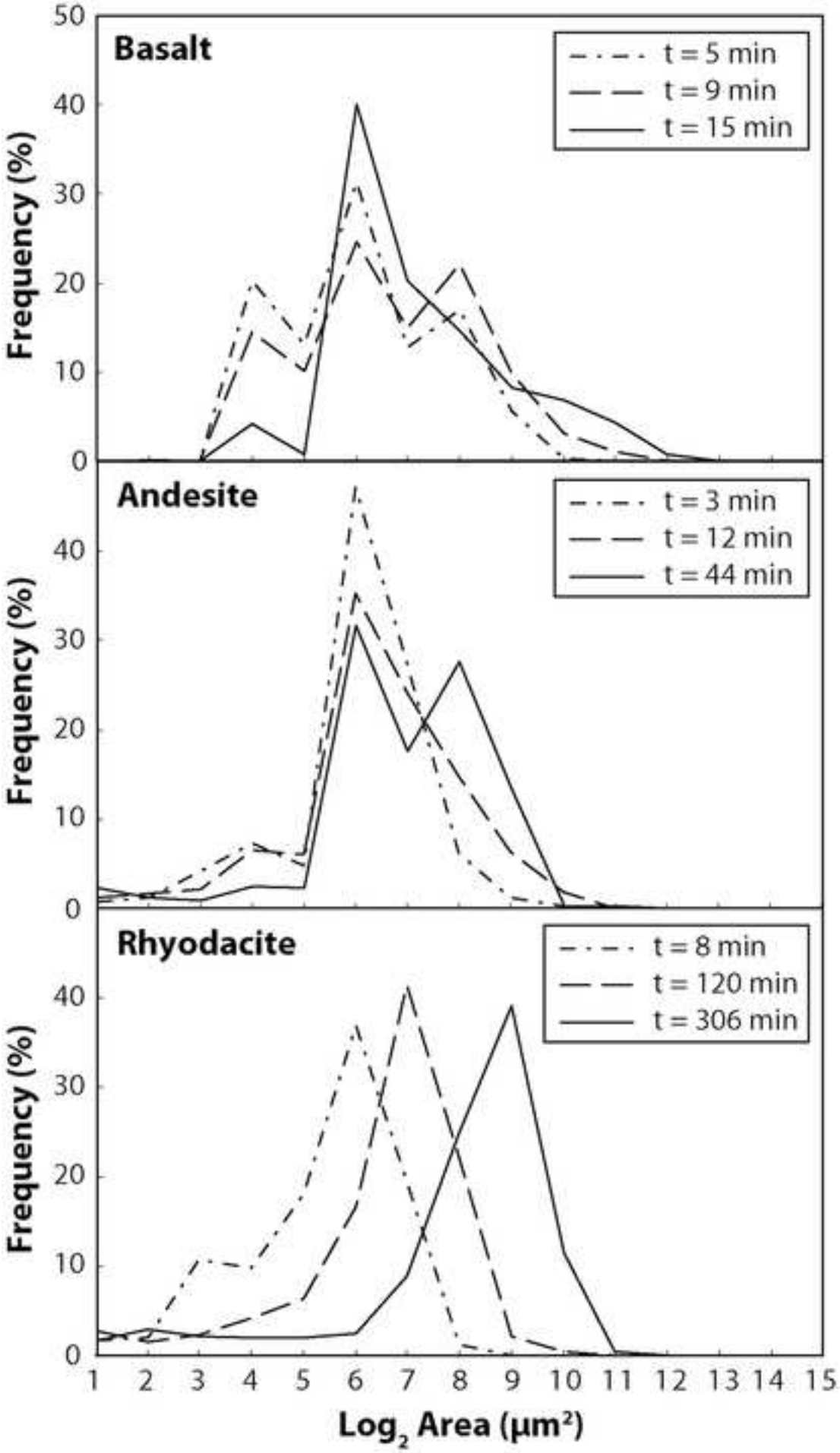

Figure 8
Click here to download high resolution image

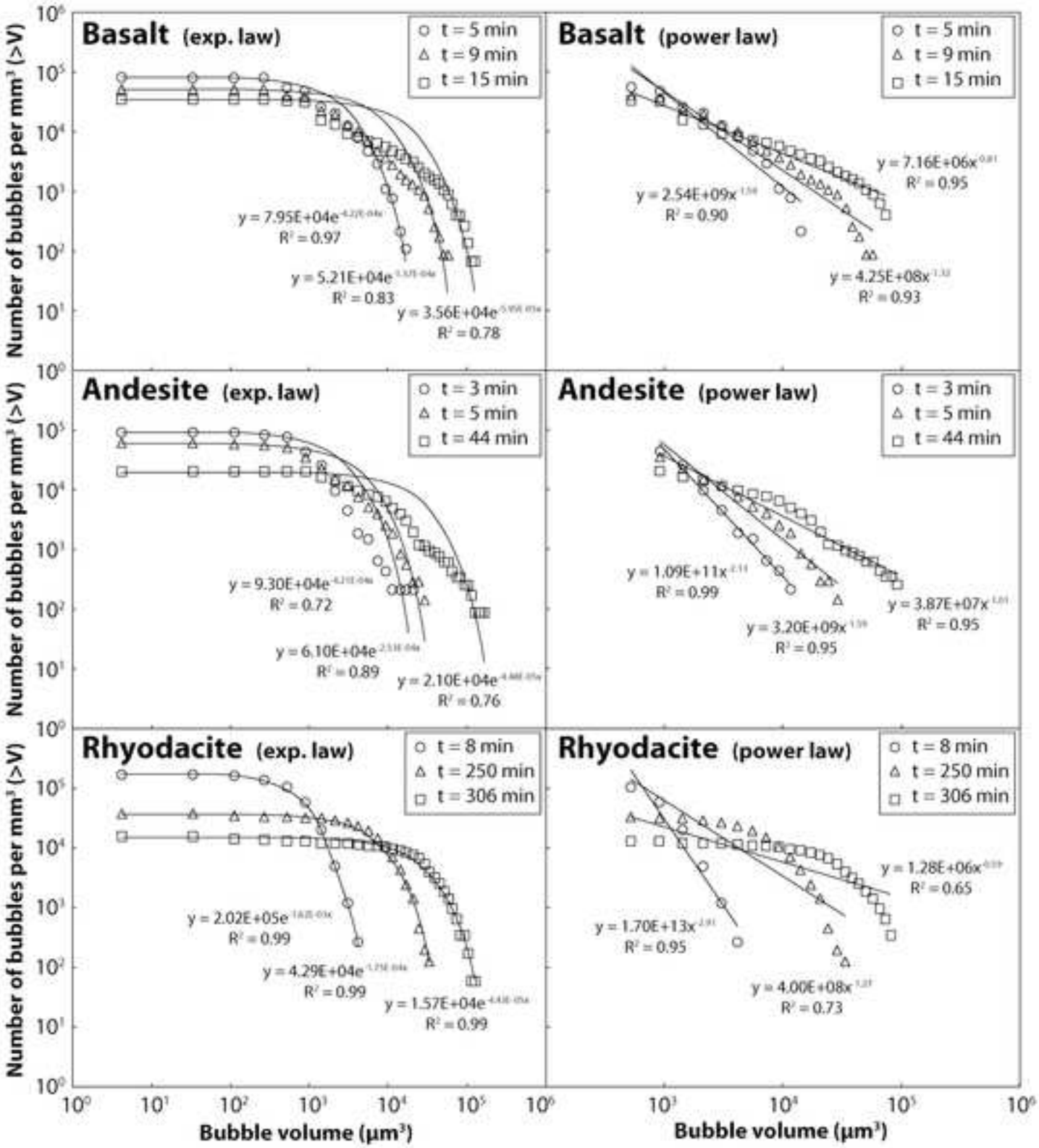

Table 1. Electron microprobe analyses of glasses used as starting material and FTIR measurements of the volatiles in the melt.

	Basalt (18) T_{exp}=1240 °C T_{liq}=1220 °C	**Andesite (17)** T_{exp}=1200 °C T_{liq}=1150 °C	**Rhyodacite (16)** T_{exp}=1100 °C T_{liq}=1090 °C
SiO_2	50.64 (0.29)	57.90 (0.44)	68.65 (0.29)
TiO_2	0.85 (0.05)	0.85 (0.08)	0.55 (0.04)
Al_2O_3	16.45 (0.22)	17.87 (0.51)	14.30 (0.15)
FeO_{tot}	-	-	3.49 (0.08)
MnO	8.08 (0.12)	5.87 (0.16)	-
MgO	7.60 (0.14)	4.21 (0.11)	1.46 (0.06)
CaO	10.39 (0.14)	6.98 (0.17)	3.95 (0.07)
Na_2O	3.27 (0.11)	3.25 (0.12)	3.61 (0.08)
K_2O	2.16 (0.07)	2.64 (0.21)	3.09 (0.09)
Total	99.45 (0.34)	99.57 (0.33)	99.10 (0.31)
H_2O (ppm)	13 (1)	19 (3)	408 (26)
CO_2 (ppm)	101 (10)	289 (29)	1135 (114)
H_2O (vol.%)[a]	17.5	23.6	84.3
CO_2 (vol.%)[a]	33.4	57.3	81.8
Bubble vol. (%)[b]	16	13	30

T_{exp}: temperature at which the experiment is performed

T_{liq}: liquidus temperature calculated using MELTS

([a]) Volume produced by the exsolution of the single volatile component present in the melt (either H_2O or CO_2) calculated at 1 atm and at different experimental temperatures, assuming an ideal behavior of the gas phase (PV=nRT). Note that these values are much greater than the total volume of the gas phase observed at the end of the experiment ([b]), indicating some volatiles remained in the melt.

Table 2. Results from image analyses.

Basalt				
Exp. time (s)	30	300	540	900
Ave. Rad. (μm)	4.06	4.68	5.72	6.96
Std. Dev.	1.14	2.37	3.35	4.84
Porosity (φ)	0.063	0.065	0.095	0.157
N_B (mm^{-3})	$8.46*10^4$	$7.92*10^4$	$5.19*10^4$	$3.55*10^4$
G_R ($mm*s^{-1}$)[a]	$1.35*10^{-4}$	$2.31*10^{-6}$	$4.32*10^{-6}$	$3.45*10^{-6}$
Andesite				
Exp. time (s)	45	165	735	2644
Ave. Rad. (μm)	4.13	5.04	5.78	9.04
Std. Dev.	1.68	2.72	2.77	4.87
Porosity (φ)	0.044	0.068	0.076	0.137
N_B (mm^{-3})	$9.33*10^4$	$6.10*10^4$	$5.37*10^4$	$2.10*10^4$
G_R ($mm*s^{-1}$)[a]	$9.18*10^{-5}$	$7.54*10^{-6}$	$1.30*10^{-6}$	$1.71*10^{-6}$
Rhyodacite				
Exp. time (s)	480	7207	14974	18394
Ave. Rad. (μm)	3.40	5.14	8.65	13.35
Std. Dev.	1.38	2.08	2.89	4.80
Porosity (φ)	0.06	0.096	0.184	0.297
N_B (mm^{-3})	$1.72*10^5$	$9.01*10^4$	$3.77*10^4$	$1.54*10^4$
G_R ($mm*s^{-1}$)[a]	$7.08*10^{-6}$	$2.59*10^{-7}$	$4.52*10^{-7}$	$1.37*10^{-6}$

([a]) Growth rate (G_R) is calculated for each segment Δt.

Electronic supplementary material

Click here to download Electronic supplementary material: Electronic Appenidx.pdf

Video

Click here to download Video: Rhyodacite_experiment.mpg